Article | Received 19 May 2026; Revised 4 July 2026; Accepted 23 July 2026; Published 18 August 2026
https://doi.org/10.55092/aimat20260009

Highly vertically oriented 2D/3D tin perovskite films for efficient and stable solar cells

Ziyong Kang[1,†,*], Mingyu Ma[2,†], Yibo Han[1], Fen Zhang[3], Lu Zhang[4,*], Jingyuan Qiao[5], Zhixin Sheng[1], Peng Feng[5,*] and Hongqiang Wang[1,*]

[1] State Key Laboratory of Solidification Processing, Center for Nano Energy Materials, School of Materials Science and Engineering, Northwestern Polytechnical University, Xi'an, China
[2] School of Physical Science and Technology, ShanghaiTech University, Shanghai, China
[3] Shaanxi Materials Analysis and Research Centre, Northwestern Polytechnical University, Xi'an, China
[4] Key Laboratory of Applied Surface and Colloid Chemistry Ministry of Education, Shaanxi Key Laboratory for Advanced Energy Devices, Shaanxi, Engineering Lab for Advanced Energy Technology, School of Materials Science Engineering Shaanxi Normal University, Xi'an, China
[5] Frontier Science Center for Flexible Electronics, Xi'an Institute of Flexible Electronics, Northwestern Polytechnical University, Xi'an, China

† These authors contributed equally to this work.

* Correspondence authors; E-mails: 2022100567@mail.nwpu.edu.cn (Z.K.); luzhang@snnu.edu.cn (L.Z.); feng@nwpu.edu.cn (P.F.); hongqiang.wang@nwpu.edu.cn (H.W.).

Highlights:

- Proposing a new strategy to regulate 2D/3D crystal orientation.
- Enhancing the crystal nucleation rate and pre-nucleation density.
- Regulating crystal orientation enhances both the efficiency and stability of the device.

Abstract: Two-dimensional/three-dimensional (2D/3D) tin perovskite solar cells (PSCs) have considerable potential for lead-free photovoltaics because of their low toxicity and favorable optoelectronic properties. However, their efficiency and stability remain limited by the difficulty of controlling the crystal orientation of 2D/3D perovskites. Here, a long-chain Lewis base molecule containing multiple functional groups, p-biguanidinobenzoic acid hydrochloride (p-BGBA), is introduced to regulate the crystallization kinetics of 2D/3D tin perovskites. The results show that p-BGBA effectively modulates the crystallization process through multiple interactions with the perovskite, thereby promoting the formation of high-quality films with a highly vertical crystal orientation. As a result, the resulting tin PSCs achieve a champion power conversion efficiency (PCE) of 14.96% and retain 91% of their initial performance after 2500 h of storage under a nitrogen atmosphere.

Keywords: perovskite solar cells; 2D/3D tin perovskite; crystal orientation; lewis base molecules

1. Introduction

Organic-inorganic halide perovskite solar cells (PSCs) are considered one of the most promising next-generation photovoltaic devices owing to their excellent optoelectronic properties, solution-processability, wide availability of raw materials, and low cost [1–5]. In recent years, the power conversion efficiency (PCE) of lead PSCs has exceeded 27% [6–8]. However, the inherent toxicity of lead and the associated environmental and health concerns remain major barriers to the large-scale deployment of these devices [9,10]. Considerable efforts have therefore been devoted to exploring environmentally friendly lead-free alternatives. Among the various candidates, tin perovskites are regarded as the most promising due to their electronic structure like that of lead perovskites, as well as their more suitable bandgap, stronger visible-light absorption, and higher carrier mobility [11–15].

Compared with lead perovskites, tin perovskites are more prone to the oxidation of Sn^{2+} to Sn^{4+} and undergo faster crystallization, often leading to high defect densities and uncontrolled crystal growth in the films, which in turn limits device photovoltaic performance [16–18]. To overcome these challenges, early studies primarily adopted solvent engineering and additive engineering strategies [19–21]. Nonetheless, their impact on oxidation resistance and long-term stability remained limited, despite some improvement in device performance. Furthermore, researchers have introduced bulky organic spacer cations to construct two-dimensional/three-dimensional (2D/3D) hybrid structures, which have been shown to not only markedly improve environmental stability but also effectively regulate crystallization [22–24]. For example, Liao *et al*. introduced phenethylammonium bromide (PEABr) to construct a 2D/3D heterojunction, reducing the Sn^{4+} content in the film to one-third of the original value and significantly improving device stability [25]. Yu *et al*. employed 4-fluorophenethylammonium bromide (FPEABr) to form a 2D/3D heterostructure, increasing the device efficiency to 14.81% and improving storage stability by approximately twofold compared with the control device [26]. Li *et al*. partially replaced PEABr with phenethylammonium thiocyanate (PEASCN), promoting the formation of highly oriented quasi-2D structures with high n values and thereby prolonging carrier lifetimes [27]. However, the crystal orientation in 2D/3D tin perovskite films remains insufficiently regulated, leading to suboptimal film quality and consequently constraining further improvement in device photovoltaic performance.

Herein, we report a multifunctional long-chain Lewis base molecule, p-biguanidinobenzoic acid hydrochloride (p-BGBA), for regulating the crystallization of 2D/3D tin perovskite films. We find that the carbonyl and guanidino groups in p-BGBA establish multiple coordination interactions with tin perovskite, enabling the simultaneous regulation of crystallization kinetics and passivation of both shallow- and deep-level defects. These synergistic effects lead to highly vertically oriented 2D/3D tin perovskite films, which in turn enhance charge transport. As a result, inverted 2D/3D tin PSCs show significantly improved PCEs from 12.37% to 14.96%, with a remarkable enhancement in the open-circuit voltage (V_{OC}) from 0.80 to 0.88 V, short-circuit current density (J_{SC}) 22.02 to 22.97 mA cm^{-2}, and fill factor (FF) 70.24% to 74.03%. Moreover, the long-term stability of tin PSCs is significantly improved, which further supports their future practical applications.

2. Result and discussion

The chemical structure and electrostatic surface potential (ESP) distribution of the p-BGBA molecule are shown in Figure S1. The electron-rich regions (negative charge) are mainly located on the carboxyl group and the C = N moiety of the guanidino group. These regions may interact with undercoordinated Sn^{2+} species as well as organic and inorganic defects through Lewis acid-base interactions, thereby significantly affecting the nucleation and growth processes of perovskite films [28,29]. The possible effects of p-BGBA molecules on the crystal orientation of 2D/3D tin perovskite films are schematically illustrated in Figure 1a. To probe the interaction between p-BGBA and the perovskite, X-ray photoelectron spectroscopy (XPS) was conducted to examine the chemical states of the perovskite surface (Figure S2). As shown in Figure 1b,c, the control film exhibits two characteristic peaks at 495.0 and 486.58 eV, assigned to Sn $3d_{3/2}$ and Sn $3d_{5/2}$, respectively [30]. Deconvolution of the Sn 3d spectra reveals Sn^{4+}/Sn^{2+} contributions of 65.2% and 48.6% in the corresponding spectral regions (Figure 1d), indicating appreciable oxidation of Sn^{2+} in the control film. After introducing p-BGBA, both peaks shift to lower binding energies, to 494.80 and 486.39 eV, respectively. Correspondingly, the fitted Sn^{4+}/Sn^{2+} contributions decrease to 32.5% and 22.4% (Figure 1d), suggesting that p-BGBA effectively suppresses the oxidation of Sn^{2+}. A similar trend is also observed for the I 3d species, with the I $3d_{3/2}$ and I $3d_{5/2}$ peaks shifting toward lower binding energies as well (Figure 1e) [31]. In addition, as shown in Figure 1f,g, compared with the control film, the binding energy of the N 1s peak in the p-BGBA treated film shifts from 400.51 eV to 400.62 eV, while the O 1s peak shifts from 530.18 eV to 530.41 eV. These results confirm that both the guanidino and carboxyl groups in p-BGBA interact with undercoordinated Sn^{2+} and the I^- ions in the $[SnI_6]^{4-}$ octahedra of the perovskite [32,33]. Moreover, the interaction between p-BGBA and the perovskite was further supported by Fourier transform infrared (FTIR) spectroscopy. As shown in Figure S3, the N-H stretching vibration shifted from 3435 to 3428 cm^{-1}, the band at 1625 cm^{-1} shifted to 1620 cm^{-1}, and the C = O stretching vibration shifted from 1669 to 1665 cm^{-1}. These peak shifts are consistent with the XPS results, further confirming the interaction between p-BGBA and the perovskite.

To further compare the steady-state optoelectronic properties of tin perovskite films without and with p-BGBA, a series of optical characterizations were carried out. As shown in Figure 2g–i, PL mapping reveals that the p-BGBA treated film exhibits an emission intensity approximately 2.5 times that of the control film, together with a more concentrated emission distribution. Consistently, time-resolved photoluminescence (TRPL) measurements show that the average carrier lifetime (τ_{ave}) increases from 18.24 ns for the control film to 31.14 ns for the p-BGBA-treated film (Figure 3a and Table S1). Meanwhile, the photoluminescence quantum efficiency (PLQE) of the perovskite films is enhanced from 8.8% to 13.8% (Figure 3b). Additionally, we measured the UV-visible absorption spectra. Figure S4 clearly shows that the bandgaps of both samples remain unchanged at 1.42 eV. Although the PL mapping shows a slight redshift after p-BGBA treatment, this small shift is more likely associated with subtle changes in the local emissive environment and carrier relaxation behavior, rather than a meaningful change in the bulk bandgap [34,35]. Furthermore, devices with an ITO/perovskite/Ag architecture were fabricated, and the corresponding current-voltage (*I-V*) characteristics were measured. The corresponding conductivity was calculated using Supplementary Equation (1) in the Supporting Information. As shown in Figure 3c, the p-BGBA treated film exhibits a steeper *I-V* curve than the control film, with

the conductivity increasing from 1.04 × 10^{-3} to 2.91 × 10^{-3} mS cm^{-1}. These results indicate that the introduction of p-BGBA effectively suppresses non-radiative recombination in the perovskite films.

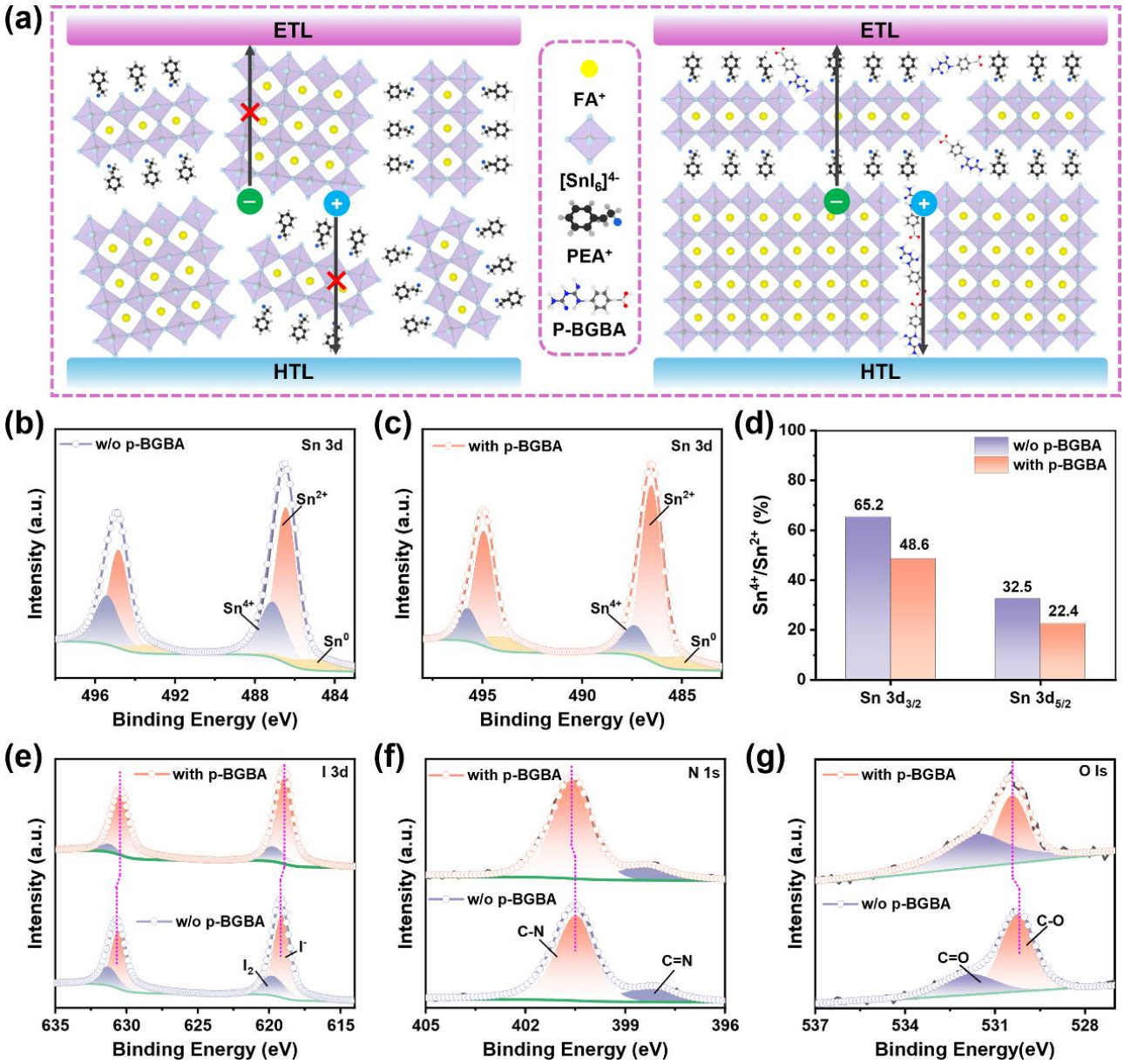

Figure 1. Structural and chemical properties of p-BGBA modified films. **(a)** Schematic illustration of the crystal orientation and charge-transport behavior of the control and p-BGBA modified perovskite films. XPS spectra of Sn for the films **(b)** without and **(c)** with p-BGBA, together with **(d)** the corresponding Sn^{4+}/Sn^{2+} ratio. XPS spectra of **(e)** I, **(f)** N, and **(g)** O for films without and with p-BGBA.

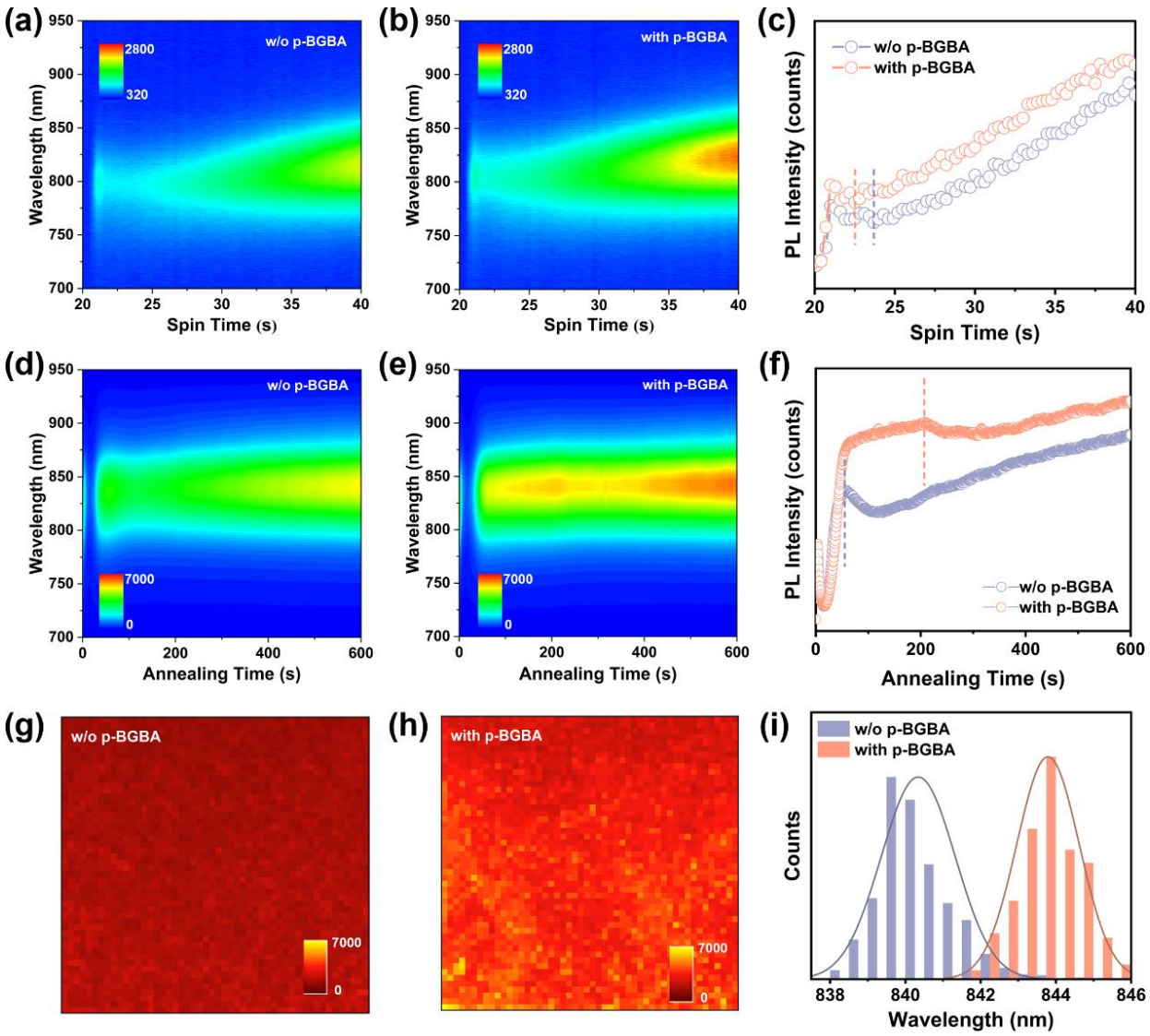

Figure 2. Optical properties of p-BGBA modified tin perovskite films. In situ photoluminescence (PL) spectra of tin perovskite films during the spin-coating process **(a)** without and **(b)** with p-BGBA, and **(c)** the corresponding evolution of PL intensity. In situ PL spectra of tin perovskite films during the annealing process **(d)** without and **(e)** with p-BGBA, and **(f)** the corresponding evolution of PL intensity. PL intensity mapping images of the perovskite films **(g)** without and **(h)** with p-BGBA, and **(i)** the corresponding statistical distribution of PL wavelength.

The effect of p-BGBA on the crystallization behavior of tin perovskite films was further examined by grazing-incidence wide-angle X-ray scattering (GIWAXS). As shown in Figure 3d–f, both films display pronounced Bragg spots. The diffraction spot at q_r = 0.32 Å^{-1} is assigned to the 2D phase (n = 2), whereas the spot at q_r = 1.0 Å^{-1} corresponds to the (100) planes of the orthorhombic 3D (n = ∞) bulk perovskite [36]. The diffraction spots are predominantly distributed along the q_z direction, indicating that the preferential crystal growth of perovskite along the (h00) orientation [37]. In addition, the slightly weakened 2D phase signal suggests that p-BGBA not only improves the orientation of the 3D phase but also regulates the distribution and orientation of the 2D phase. This behavior may originate from the strong coordination between p-BGBA and $[SnI_6]^{4-}$ octahedra, which preferentially promotes 3D phase growth during crystallization. As reported in our previous work,

such a regulated 2D/3D phase arrangement is favorable for charge transport, further supporting the proposed mechanism [28]. Moreover, the Hermans orientation factor (HF) was calculated from the polar intensity profiles along the (100) diffraction ring within the (q) range of 0.95–1.05 $Å^{-1}$. According to Supplementary Equations (2)–(3) in the Supporting Information, the HF increased from 0.49 to 0.81 after the incorporation of p-BGBA, indicating a substantially enhanced out-of-plane orientational order of the (100) planes. Additionally, X-ray powder diffraction (XRD) measurements reveal a markedly enhanced crystallinity for the p-BGBA-treated film (Figure S5), further supporting the p-BGBA induced improvement in crystal orientation. To further visualize the facet orientation difference, pole figure measurements were performed along the (100) crystallographic direction (Figure S6). The results confirm that the p-BGBA treated perovskite films exhibit a more intense and concentrated signal, indicating a systematically enhanced preferred orientation. The scanning electron microscopy (SEM) images shown in Figures S7 and S8 further corroborates this conclusion. In the control film, obvious pinholes are observed on the surface, whereas the p-BGBA treated film exhibits a much denser and more compact morphology. A similar trend is evident in the cross-sectional SEM images, where noticeable voids are present between grains in the control film, while the p-BGBA treated film shows more tightly packed grains. Consistently, atomic force microscopy (AFM) measurements show that the root-mean-square roughness (RMS) decreases from 19.2 nm for the control film to 16.5 nm after p-BGBA treatment (Figure S9), indicating a smoother film surface. Such a morphology is expected to promote more intimate interfacial contact between the perovskite and the electron transport layer (ETL). Collectively, these results demonstrate that p-BGBA effectively improves the crystal orientation and film quality of the perovskite layer.

To gain deeper insight into the ultrafast transport dynamics of photoexcited carriers across the perovskite films on the picosecond timescale, femtosecond transient absorption (fs-TA) measurements were further performed on the perovskite films. As shown in Figure 3g,h, both the control and p-BGBA treated films exhibit two distinct ground-state bleaching (GSB) features centered at ~660 and ~835 nm, which are assigned to the transient bleaching signals of the 2D and 3D perovskite phases, respectively [30]. In general, the GSB intensity reflects the population of photogenerated carriers in the conduction and valence bands of the perovskite, and hence the charge transfer dynamics can be directly evaluated by monitoring the quenching kinetics of the GSB signals [37–39]. Compared with the GSB signals of the control film, the p-BGBA treated film exhibits markedly enhanced intensities for both the 2D and 3D features. This evolution is attributed to the improved crystal orientation of the film. The more pronounced enhancement of the 2D signal relative to the 3D signal may be associated with the limited film thickness used for the TA measurements, as well as the later crystallization of the 2D phase. The GSB decay kinetics were further fitted with a triple-exponential function (Supplementary Equations (4)–(5) in the Supporting Information) to better elucidate the charge-transfer and carrier-recombination dynamics. As shown in Figure 3i, Figure S10 and Table S2, compared with the control perovskite film, the lifetime of the 3D phase in the p-BGBA treated film increases from 101.32 ps to 148.82 ps, while that of the 2D phase increases from 136.93 ps to 158.52 ps. These results further support that p-BGBA modulates the crystallization process, thereby improving the crystal orientation of the perovskite and facilitating carrier transport.

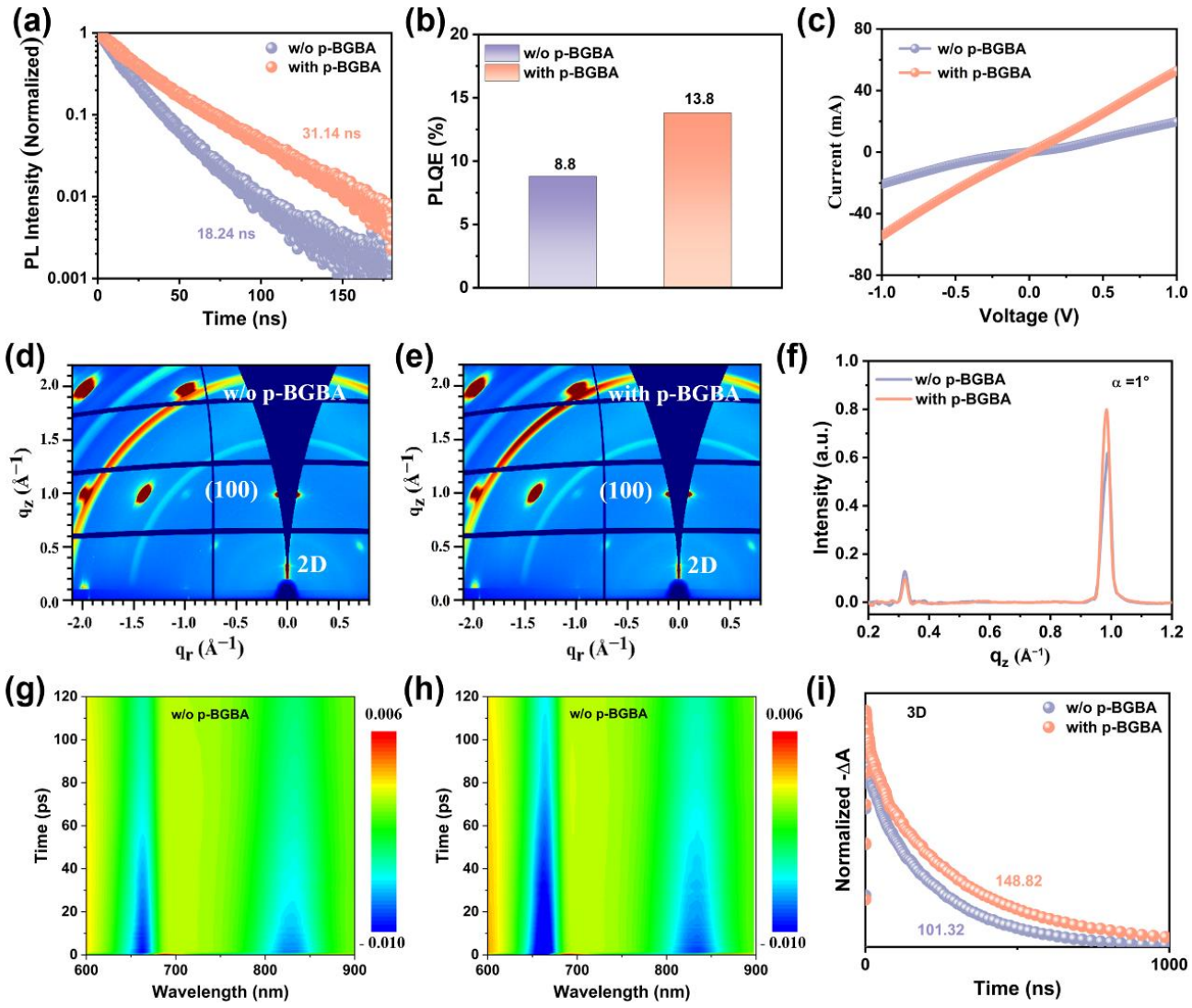

Figure 3. Optoelectronic properties and structural dynamics of p-BGBA modified films. **(a)** Time-resolved photoluminescence; **(b)** PLQE, and **(c)** current-voltage (*I-V*) curves of devices without and with p-BGBA. GIWAXS patterns at different depths for tin perovskite films **(d)** without and **(e)** with p-BGBA, and **(f)** the corresponding azimuthal integration plots. Pseudocolor transient absorption (TA) spectra of perovskite films **(g)** without and **(h)** with p-BGBA, and **(i)** the corresponding dynamic TA decay of the 3D phase.

To evaluate the device performance, tin PSCs were fabricated with the ITO/PEDOT:PSS/Perovskite/PCBM/BCP/Ag configuration, as illustrated in Figure 4a,b shows the champion current density-voltage (*J-V*) curves of the devices based on the control and p-BGBA treated perovskite films. The control tin PSC exhibits a PCE of 12.37%, with a V_{OC} of 0.80 V, an FF of 70.24%, and a J_{SC} of 22.02 mA cm^{-2}. After introducing p-BGBA, the device performance is markedly improved, delivering a PCE of 14.96%, along with an increased V_{OC} of 0.88 V, an FF of 74.03%, and a J_{SC} of 22.97 mA cm^{-2}. In addition, the external quantum efficiency (EQE) spectra shown in Figure 4c reveals that the integrated current density is in good agreement with the J_{SC} value obtained from the *J-V* measurements. Furthermore, the target device shows a steady state PCE output of 14.44% under a constant bias voltage of 0.68 V, while the control device achieves a steady state PCE of only 11.54% at 0.62 V, as shown in Figure S11. To assess the general applicability of p-BGBA regulation and the reproducibility of the

fabrication process, the photovoltaic parameters of devices fabricated across 15 independent batches were statistically analyzed. As shown in Figure S12, the p-BGBA modified tin perovskite solar cells consistently exhibit improved photovoltaic parameters relative to the control devices. Notably, the PCE values show a narrower distribution, demonstrating that p-BGBA modification not only enhances device performance but also improves the reproducibility of perovskite film formation and device fabrication.

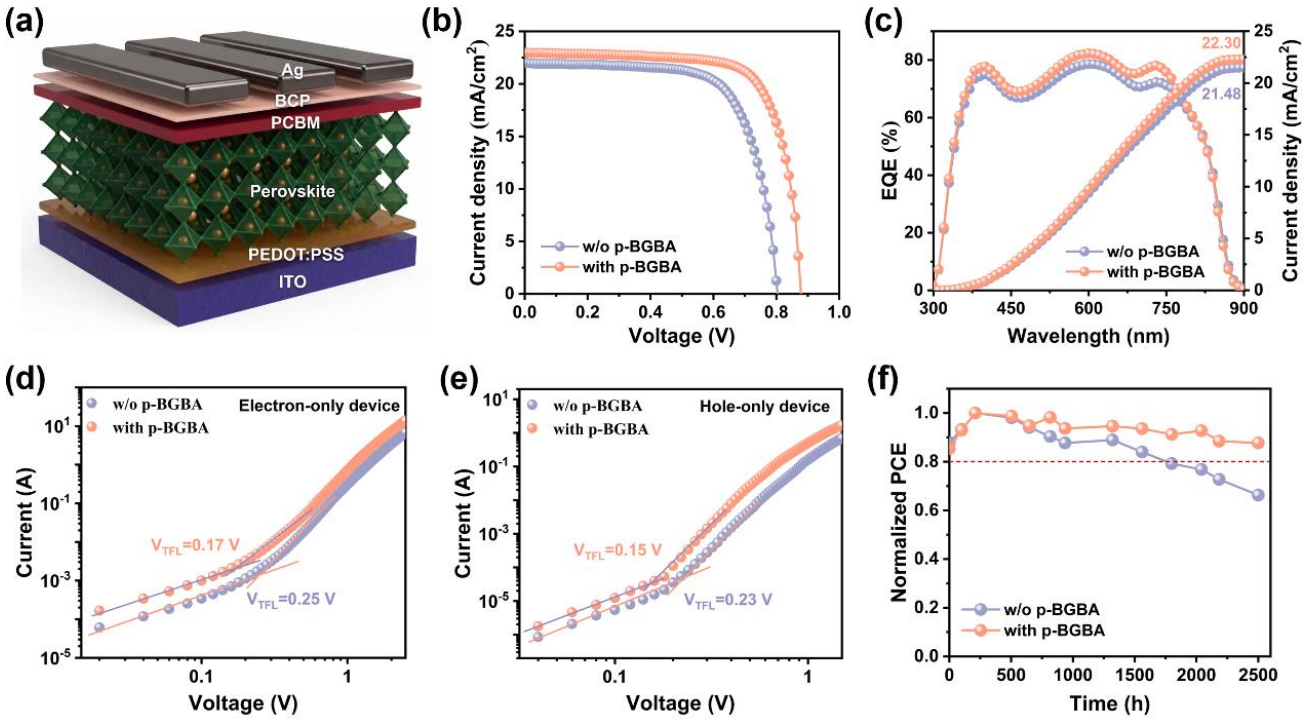

Figure 4. Photovoltaic performance and stability of p-BGBA modified tin PSCs. **(a)** Schematic illustration of the device structure of tin PSCs; **(b)** current density-voltage (*J-V*) curves of the champion tin PSCs without and with p-BGBA; **(c)** EQE spectra of the corresponding tin PSCs. Dark J–V curves of the **(d)** electron-only and **(e)** hole-only devices. **(f)** Long-term shelf stability of tin PSCs without and with p-BGBA under an N_2 atmosphere.

Moreover, the defect-state densities of the control and p-BGBA treated perovskites were quantified by the space-charge-limited current (SCLC) method. Electron-only devices with an ITO/SnO_2/perovskite/PCBM/Ag architecture and hole-only devices with an ITO/PEDOT:PSS/perovskite/Spiro-OMeTAD/Ag architecture were fabricated, as shown in Figure 4d,e. The trap density (N_t) was determined using Supplementary Equation (6) in the Supporting Information. Compared with the control device, the p-BGBA treated device exhibits a reduced electron trap density from 1.42×10^{16} to 9.70×10^{15} cm^{-3}, together with a decrease in hole trap density from 1.31×10^{16} to 8.54×10^{15} cm^{-3}. These results further verify that p-BGBA effectively lowers the defect density and suppresses non-radiative recombination by regulating the crystal orientation of the perovskite film, which should also contribute to improved device stability. Finally, the storage stability of the two devices was evaluated in an unencapsulated state under dark conditions in an N_2 filled glovebox at approximately 25 ℃, where both the H_2O and O_2 levels were maintained below 0.1 ppm. As shown in Figure 4f, the control device retained less than 80% of its initial PCE after 1750 h of storage. By contrast, the device incorporating p-BGBA still maintained 91% of its initial PCE after 2500 h.

3. Conclusion

In summary, we employed the multifunctional molecule p-BGBA to regulate the crystal orientation of 2D/3D tin perovskites, achieving efficient and stable tin PSCs. By establishing multiple coordination interactions with the perovskite components, p-BGBA effectively regulates crystallization, lowers the defect density, and consequently improves film crystal orientation as well as charge separation and extraction. As a result, the device PCE is significantly increased from 12.37% to 14.96%. Meanwhile, the p-BGBA-based device retains 91% of its initial PCE after 2500 h of storage under a nitrogen atmosphere, demonstrating markedly improved stability. This work provides a simple and effective pathway to improve crystal orientation and facilitate charge transport, offering valuable guidance for the development of efficient and stable tin PSCs.

4. Experimental section

4.1. Materials

Formamidinium iodide (FAI, 99.5%) and phenethylammonium Chloride (PEACl, 99.5%) were purchased from Xi'an Yuri Solar Co. Ltd. p-BGBA was purchased from Xi'an e-Light New Material Co., Ltd. Tin (II) iodide (SnI_2, 99.999%) was purchased from 3A Materials, Tin(II) Fluoride (SnF_2, 99.9%), Tin powder (99.5%), and Ammonium thiocyanate (NH_4SCN, 99.99%) were purchased from Aladdin, 1-(3-methoxycarbonyl)-propyl-1-phenyl-(6, 6) C61 (PCBM) and bathocuproine (BCP) were purchased from 3A Nano-C, respectively. Tin (IV) oxide (SnO_2, 99%) was purchased from Alfa Aesar, 2,2',7,7'-Tetrakis N, N-di(4-methoxyphenyl) amino]-9,9'-spirobifluorene (Spiro-MeOTAD, 99%), Dimethyl sulfoxide (DMSO, 99.9%), N, N-dimethylformamide (DMF, 99.8%), Iso-Propyl Alcohol (IPA, 99.5%), and chlorobenzene (CB, 99.8%) were obtained from Sigma-Aldrich. PEDOT: PSS (Chevios Al4083) was purchased from J&K Chemical. All the above chemicals were used as received without any further purification. Toluene (99.8%) was purchased from Ourchem and contained with a molecular sieve to remove water.

4.2. Precursor solution

The perovskite precursor solution ($PEA_{0.15}FA_{0.85}SnI_{2.85}Cl_{0.15}$) was prepared by dissolving 65.79 mg FAI (0.3825 mmol), 10.64 mg PEACl (0.0675 mmol), 167.63 mg SnI_2 (0.45 mmol), 7.05 mg SnF_2 (0.09 mmol), 1.71 mg NH_4SCN (0.0225 mmol), 2.81 mg Sn powder (0.0225 mmol) and different concentrations of p-BGBA, into a mixed solvent of 100 μL DMSO and 400 μL DMF and then stirring for about 12 h.

4.3. Device fabrication

The tin PSCs were fabricated with a configuration of ITO/PEDOT: PSS/perovskite/PCBM/BCP/Ag. ITO glass substrates were ultrasonically cleaned with detergent, deionized water, ethyl alcohol, acetone, and isopropanol for 60 min, respectively. Then, the cleaned ITO glass substrates were cleaned with oxygen plasma (Harrick PDC-32G) for 20 min. PEDOT: PSS was spin-coated on ITO substrates at 5000 rpm for 45 s and annealed at 140 ℃ for 20 min in air. After cooling, the tin perovskite precursor solution was spun at 1000 rpm for 10 s, followed by 5000 rpm for 30 s in the glove box. Toluene was dripped onto

the perovskite film 10 s after the rotation speed was increased to 5000 rpm, following with annealing at 70 ℃ for 10 min. Then, the electron transport layer was prepared by spin-coating the PCBM solution (30 mg/mL in CB) at 1800 rpm for 30 s and annealed at 70 ℃ for 10 min. Finally, a 5 nm thick BCP and 110 nm thick Ag was deposited using a vacuum thermal coater (Suzhou Fang Sheng OMV-FS200). The size of the tin PSCs is 0.05 cm^2, which is determined by the overlapping area of the ITO and Ag contact.

4.4. Devices characterization

The XRD patterns were determined by an X-ray diffractometer (AXS D8 Advanced, Bruker, Germany) with monochromatic Cu Kα radiation. The morphology of the perovskite film was measured by a field emission scanning electron microscope (SEM) (ZEISS Sigma 300, Germany). Atomic force microscopy (AFM) was performed using Dimension Icon microscope (Bruker, Germany). Ultraviolet-visible (UV-vis) absorption measurement was obtained by the UV-LAMBDA 365 spectrophotometer. The PL were characterized using an Edinburg Instruments FLS 980. Microscopic PL mappings were taken with a confocal spectroscopic system (South Port, Jade Mat), where a 532 nm continuous-wave laser was used as the excitation source together with a◊50 objective lens (NA = 0.8). The TRPL spectra were collected using a Delta Flex modular fluorescence lifetime system by Horiba Scientific. The X-ray photoelectron spectroscopy was tested by the PHI-5000 Versa Probe III. The *J-V* curves were measured using a Xenon-lamp-based solar simulator (Oriel 67005, 150 W Solar Simulator) with a source meter (Keithley 2420 Source-Meter) under illumination at AM 1.5G (100 mW cm^{-2}). The light intensity was calibrated with a monocrystalline silicon reference cell (Hamamatsu S1133). All the devices were tested in a nitrogen-filled glovebox. The external quantum efficiency (EQE) was characterized by using an Enlitech EQE measurement system (QE-R3011). A Keithley 2420 Source-Meter was used to measure the relevant *I-V* curves. GIWAXS measurement was performed by employing a beam energy of 10 keV and a PILATUS detector at the BL02U2 and BL03HB beamline of Shanghai Synchrotron Radiation Facility (SSRF), Shanghai, China. In situ fluorescence spectra were recorded in a N_2 glovebox, and the excited light was at 365 nm from a UV lamp. TA spectra measurements were conducted by utilizing a TA system (Time-Tech Spectra, LLC) equipped with a high-speed spectrometer (Ultrafast systems, HELIOS) and a regeneratively amplified laser (Light conversion, 1030 nm, 230 fs and 100 kHz repetition). The diode-pumped all-solid-state femtosecond Yb: YAG laser is equipped with a wavelength of 1030 nm, a matching repetition frequency of 100 kHz, and a pulse width of 230 fs. TA measurements were performed using a 530 nm excitation laser at an excitation power of 1 mW. The excitation beam was directed onto the perovskite film from the substrate side.

Supplementary data

The authors confirm that the supplementary data is available within this article. This supporting material provides supplementary data and detailed characterization results that support the main findings of this work. It includes the molecular structure and electrostatic potential distribution of p-BGBA (Figure S1), full XPS spectra of perovskite films before and after p-BGBA incorporation (Figure S2), FTIR spectra (Figure S3), UV–vis absorption spectra (Figure S4), XRD patterns (Figure S5), polar diagrams of the (100) crystal facet (Figure S6), SEM images (Figure S7), cross-sectional SEM images (Figure S8), AFM images (Figure S9), dynamic transient absorption (TA) decay of the 2D phase Figure S10), steady-state

power output at the maximum power point (Figure S11), and statistical analysis of the corresponding device efficiencies (Figure S12). Furthermore, Table S1 summarizes the TRPL fitting parameters, while Table S2 presents the TA fitting parameters. These supplementary results collectively demonstrate that p-BGBA effectively regulates the vertical orientation of 2D/3D tin perovskite films and contributes to the improved optoelectronic performance of the corresponding devices.

Data availability statement

The data or datasets that support the findings of this study are available from the corresponding author upon reasonable request.

Declaration of generative AI and AI-assisted technologies

The authors did not use generative AI or AI-assisted technologies in the writing of this manuscript. The author takes full responsibility for the content of the manuscript.

Acknowledgments

Funding: this work was financially supported by the National Natural Science Foundation of China (No. 12404463).

Authors' contribution

Conceptualization, Z.K.; methodology, Z.K., M.M. and Y.H.; software, Z.K.; validation, P.F. and H.W.; formal analysis, Z.K., Y.H. and P.F.; investigation, F.Z., L.Z., J.Q. and Z.S.; resources, Z.K., P.F. and H.W.; data curation, Z.K.; writing—original draft preparation, Z.K., P.F. and M.M.; writing—review and editing, Z.K. and H.W.; visualization, F.Z., Y.H. and Z.S; supervision, H.W.; project administration, P.F. and H.W.; funding acquisition, Z.K., P.F. and H.W. All authors have read and agreed to the published version of the manuscript.

Conflicts of interest

There are no conflicts to declare.

References

[1] Liu S, Li J, Xiao W, Chen R, Sun Z, *et al*. Buried interface molecular hybrid for inverted perovskite solar cells. *Nature* 2024, 632(8025):536–542.

[2] Fei C, Zhang Y, Wang M, Yang Y, Shi X, *et al*. Limiting phosphonic acid interlayer–perovskite reactivity to stabilize perovskite solar modules. *Science* 2026, 391(6780): eadz7969.

[3] Yang Y, Chen H, Liu C, Xu J, Huang C, *et al*. Amidination of ligands for chemical and field-effect passivation stabilizes perovskite solar cells. *Science* 2024, 386(6724):898–902.

[4] Zhu T, Song Z, Yan Y, Li C. Pyrene-based molecular contacts inspire perovskite solar cells. *Green Carbon* 2025, 3(2):170–171.

[5] Huo X, Lv J, Wang K, Sun W, Liu W, *et al*. Surface sulfidation constructing gradient heterojunctions for high-efficiency (approaching 18%) HTL-free carbon-based inorganic perovskite solar cells. *Carbon Energy* 2024, 6(12):e586.
[6] Gao D, Lu S, Zhang C, Wang N, Yu Z, *et al*. Autonomous closed-loop framework for reproducible perovskite solar cells. *Nature* 2026, 653(8115):707–714.
[7] Bi L, Wang J, Zeng Z, Ji X, Huang X, *et al*. Temperature-controlled vacuum quenching for perovskite solar modules towards scalable production. *Nat. Photonics* 2025, 19(9):968–976.
[8] Zhang Z, Zhu R, Li G, Tang Y, Wu H, *et al*. Photoswitchable isomers to improve grain boundary resilience and perovskite solar cells stability under light cycling. *Nat. Energy* 2026, 11(4):623–632.
[9] Maietta I, Otero-Martínez C, Fernández S, Sánchez L, González-Fernández Á, *et al*. The toxicity of lead and lead-free perovskite precursors and nanocrystals to human cells and aquatic organisms. *Adv. Sci*. 2025, 12(13):2415574.
[10] Li J, Cao H, Jiao W, Wang Q, Wei M, *et al*. Biological impact of lead from halide perovskites reveals the risk of introducing a safe threshold. *Nat. Commun*. 2020, 11:310.
[11] Kahmann S, Nazarenko O, Shao S, Hordiichuk O, Kepenekian M, *et al*. Negative thermal quenching in $FASnI_3$ perovskite single crystals and thin films. *ACS Energy Lett*. 2020, 5(8):2512–2519.
[12] Chowdhury TH, Reo Y, Yusoff ARBM, Noh YY. Sn-based perovskite halides for electronic devices. *Adv. Sci*. 2022, 9(33):2203749.
[13] Tao S, Schmidt I, Brocks G, Jiang J, Tranca I, *et al*. Absolute energy level positions in tin- and lead-based halide perovskites. *Nat. Commun*. 2019, 10:2560.
[14] Sanchez-Diaz J, Sánchez RS, Masi S, Krečmarová M, Alvarez AO, *et al*. Tin perovskite solar cells with > 1300 h of operational stability in N_2 through a synergistic chemical engineering approach. *Joule* 2022, 6(4):861–877.
[15] Li T, Luo X, Wang P, Li Z, Li Y, *et al*. Tin-based perovskite solar cells with a homogeneous buried interface. *Nature* 2025, 648(8092):84–90.
[16] Lanzetta L, Webb T, Zibouche N, Liang X, Ding D, *et al*. Degradation mechanism of hybrid tin-based perovskite solar cells and the critical role of tin(IV) iodide. *Nat. Commun*. 2021, 12:2853.
[17] Pitaro M, Tekelenburg EK, Shao S, Loi MA. Tin halide perovskites: from fundamental properties to solar cells. *Adv. Mater*. 2022, 34(1):2105844.
[18] Chen J, Luo J, Hou E, Song P, Li Y, *et al*. Efficient tin-based perovskite solar cells with trans-isomeric fulleropyrrolidine additives. *Nat. Photonics* 2024, 18(5):464–470.
[19] Di Girolamo D, Pascual J, Aldamasy MH, Iqbal Z, Li G, *et al*. Solvents for processing stable tin halide perovskites. *ACS Energy Lett*. 2021, 6(3):959–968.
[20] Hao F, Stoumpos CC, Guo P, Zhou N, Marks TJ, *et al*. Solvent-mediated crystallization of $CH_3NH_3SnI_3$ films for heterojunction depleted perovskite solar cells. *J. Am. Chem. Soc*. 2015, 137(35):11445–11452.
[21] Tang W, Liu T, Zhang M, Yuan F, Zhou K, *et al*. The roles of metal oxidation states in perovskite semiconductors. *Matter* 2023, 6(11):3782–3802.
[22] Chang X, Liu Y, Ping Y, Wu N, Yang T, *et al*. Multivalent ligands regulate dimensional engineering for inverted perovskite solar modules. *Science* 2026, 391(6781):153–159.
[23] Grancini G, Nazeeruddin MK. Dimensional tailoring of hybrid perovskites for photovoltaics. *Nat. Rev. Mater*. 2019, 4(1):4–22.

[24] Wang F, Jiang X, Chen H, Shang Y, Liu H, *et al*. 2D-quasi-2D-3D hierarchy structure for tin perovskite solar cells with enhanced efficiency and stability. *Joule* 2018, 2(12):2732–2743.
[25] Liao Y, Liu H, Zhou W, Yang D, Shang Y, *et al*. Highly oriented low-dimensional tin halide perovskites with enhanced stability and photovoltaic performance. *J. Am. Chem. Soc.* 2017, 139(19):6693–6699.
[26] Yu B, Chen Z, Zhu Y, Wang Y, Han B, *et al*. Heterogeneous 2D/3D tin-halides perovskite solar cells with certified conversion efficiency breaking 14%. *Adv. Mater*. 2021, 33(36):2102055.
[27] Li H, Zang Z, Wei Q, Jiang X, Ma M, *et al*. High-member low-dimensional Sn-based perovskite solar cells. *Sci. China Chem*. 2023, 66(2):459–469.
[28] Kang Z, Feng P, Wang K, Zhang L, Meng R, *et al*. Synchronous dimension-crystallization engineering enables highly efficient 2D/3D tin perovskite solar cells. *Energy Environ. Sci*. 2025, 18(9):4108–4119.
[29] Chen Y, Wang K, Chen W, Li T, Tu H, *et al*. Defects mitigation and charge transport promotion via a multifunctional Lewis base for efficient 2D/3D tin perovskite solar cells. *Adv. Energy Mater*. 2025, 15(22):2406024.
[30] Azaden A, Bhatt P, Liu Y, Wei J, Haque SA, *et al*. Toward reliable XPS analysis of tin halide perovskites. *Cell Rep. Phys. Sci.* 2026, 7(4):103228.
[31] Fajal S, Mandal W, Torris A, Majumder D, Let S, *et al*. Ultralight crystalline hybrid composite material for highly efficient sequestration of radioiodine. *Nat. Commun*. 2024, 15:1278.
[32] Wang S, Wu C, Wu T, Yao H, Hua Y, *et al*. π-Conjugated Lewis base for efficient tin halide perovskite solar cells with retarded Sn2+ oxidation. *ACS Energy Lett.* 2024, 9(3):1168–1175.
[33] Li F, Deng X, Shi Z, Wu S, Zeng Z, *et al*. Hydrogen-bond-bridged intermediate for perovskite solar cells with enhanced efficiency and stability. *Nat. Photonics* 2023, 17(6):478–484.
[34] Kang Z, Tong Y, Wang K, Chen Y, Yan P, *et al*. Tailoring low-dimensional phases for improved performance of 2D–3D tin perovskite solar cells. *ACS Mater. Lett.* 2023, 6(1):1–9.
[35] Chen Y, Tong Y, Yang F, Li T, Li W, *et al*. Modulating nucleation and crystal growth of tin perovskite films for efficient solar cells. *Nano Lett.* 2024, 24(18):5460–5466.
[36] Kang Z, Wang K, Zhang L, Yang Y, Wu J, *et al*. Homogenizing the low-dimensional phases for stable 2D–3D tin perovskite solar cells. *Small* 2024, 20(43):2402028.
[37] Liu G, Zhong Y, Feng W, Yang M, Yang G, *et al*. Multidentate chelation heals structural imperfections for minimized recombination loss in lead-free perovskite solar cells. *Angew. Chem. Int. Ed.* 2022, 61(40):e202209464.
[38] Han GR, An MN, Jang H, Han NS, Kim J, *et al*. In situ and real-time ultrafast spectroscopy of photoinduced reactions in perovskite nanomaterials. *Nat. Commun.* 2025, 16:4956.
[39] Chen X, Kamat PV, Jan áky C, Samu GF. Charge transfer kinetics in halide perovskites: on the constraints of time-resolved spectroscopy measurements. *ACS Energy Lett*. 2024, 9(6):3187–3203.